Journal of Inorganic and Organometallic Polymers and Materials (2022) 32:297–310
https://doi.org/10.1007/s10904-021-02120-z

Enhanced Photo-Catalytic and Antibacterial Properties of Ni-Doped $Cd_{0.9}Zn_{0.1}S$ Nanostructures

S. Jothi[1] · Rane Caroleena Ganesh[2] · S. Muthukumaran[3] · S. K. Rathiha[3] · R. K. Seenivasan[4]

Received: 24 July 2021 / Accepted: 1 October 2021 / Published online: 7 October 2021

Abstract

The present work describe the synthesis of $Cd_{0.9}Zn_{0.1}S$ and $Cd_{0.87}Zn_{0.1}Ni_{0.03}S$ nanostructures by chemical co-precipitation method. The XRD profile proved the cubic crystal structure of the samples without any impurity related phases. The reduced size from 63 to 51 Å and the dissimilarities in lattice parameters and micro-strain has been discussed by Ni addition in $Cd_{0.87}Zn_{0.1}Ni_{0.03}S$ structure. The noticed anomalous optical studies and the elevated transmittance at Ni doped sample suggested them for the fabrication of efficient opto-electronic devices. The energy gap reduction during the substitution of Ni = 3% is explained by the generation of extra energy levels associated with defects within the two bands. The release of additional charge carriers, improved optical property, reduced particle size and more defect generation are responsible for the enhanced photo-catalytic performance of Ni doped $Cd_{0.9}Zn_{0.1}S$. The enhanced anti-bacterial capacity in $Cd_{0.87}Zn_{0.1}Ni_{0.03}S$ is described by the collective response of reduced particle size and higher reactive oxygen species (ROS) like $O_2^{\cdot -}$, H_2O_2 and $OH^{\cdot}$ generating capacity.

Keywords Ni-doped $Cd_{0.9}Zn_{0.1}S$ · XRD · Energy gap · Photo-catalytic · MB dye · Antibacterial study

1 Introduction

Metal sulfide (MS) nanomaterials are effective photo-catalyst to develop the better organic conversions, energy demands and also environmental purposes by sun light radiation [1–5]. The semiconducting materials like ZnO, ZnS, SnO_2, etc. with band gap ≈ 3–3.7 eV exhibit good absorption along UV radiation (below 400 nm) but not good for visible radiation and hence they have limited realistic applications [6–9]. To avoid the difficulties in real-time applications, the researchers attempted to vary the size and characters of photo-catalyst using metal based nanoparticles and also the composite of semiconductors [10, 11].

✉ S. Muthukumaran
drsmk123@yahoo.co.in

1 Department of Chemistry, Government Arts College for Women, Sivagangai, Tamilnadu 630 562, India

2 Department of Chemistry, Sidharth College, Badlapur, University of Mumbai, Mumbai, Maharashtra, India

3 PG & Research Department of Physics, Government Arts College, Melur, Madurai, Tamilnadu 625106, India

4 Department of Chemistry, Government Arts College, Melur, Madurai, Tamilnadu 625106, India

In the different semiconducting materials, CdS is an outstanding material for different applications [12, 13] and employed as a excellent antibacterial agent [14]. Moreover, the physical and chemical related properties of CdS can be easily tuned using doping of metal ions [15–18], the antibacterial and photo-catalytic performance can also be improved by doping suitable metal ions. TM ions added CdS get huge attraction by its better physical and chemical nature [19, 20] and potential applications [21]. In the different TM ions Zn^{2+} is an initial dopant because it has smaller ionic radius than Cd^{2+} and so Zn^{2+} can go into CdS lattice easily and restore Cd^{2+} ions by elevating its properties [22].

The primary doping of Zn increases the E_g of CdS [23]. The higher surface area is useful to improve both the stability and photo-catalytic activity which is done by Zn in CdS [24]. Moreover, the positive effect is produced during the hybridization of Zn into CdS. Short circuit current of CdS solar cell is improved by Zn addition in CdS [25]. In the present work, Zn doping level is optimized as 10% ($Cd_{0.9}Zn_{0.1}S$) due to its better photoluminescence and structural properties based on our previous work [26].

The doping of 2nd metal ion from TM group is useful to improve the optical, structural and photo-catalytic properties $Cd_{0.9}Zn_{0.1}S$ nanostructures. Within the different TM ions,

the ions with 3d electrons create the various deep energy levels in Cd–S lattice [18]. The stimulation of deep energy levels is technologically important in luminescent devices. The increased optical absorption in the visible region by the addition Ni^{2+} makes the Ni doped $Cd_{0.9}Zn_{0.1}S$ nanostructures as a good catalyst for photo-degradation under solar irradiation [27]. E_g of CdS is reduced by Ni addition [28]. Ni^{2+} ions enclose 8 'd' electrons which makes the strong p-d hybridization [29] in Ni/Zn-CdS lattice. Since the ionic radius of Ni^{2+} (0.069 nm) is smaller than Cd^{2+} (0.097 nm) and also the electro-negativity (1.91 Pauling) is greater than Cd^{2+} (1.61 Pauling) [30], the inclusion of Ni produces more number of charge carriers and hence increased the conductivity.

Zn and Cu dual doped CdS is useful for the solar power generation and also for solar hydrogen generation. The Zn doped CdS PEC solar cell exhibits better hydrogen production capacity still at a low voltage bias of 0.1 V/SCE [31]. Kamran et al. [32] revealed the improved IR emission in Ni doped CdS which is helpful for the nano-scale light sources. The decreasing energy gap from 2.36 to 2.29 eV by the Ni doping in CdS was noticed by Sankar et al. [33]. Moreover, the photo-catalytic degradation efficiency around 94% was achieved in Ni doped CdS for MO dye for 75 min. Garmim et al. [34] described the preparation and structural characterization of Ni, Mg dual doped CdS thin films by spin coating method. They found the increased E_g from 2.42 to 2.49 eV by Mg addition up to 5 wt%. Increased photo-catalytic stability and antibacterial activities were found by Raju et al. [35] in Ni added $Cd_{0.9}Zn_{0.1}S$ nanostructure and they explained the enhancement by the combined effect of smaller size and ROS (reactive oxygen species) generating ability.

Sakthivel et al. [36] reported the addition of Ni^{2+} into Cd–Zn–S enhanced the optical transmittance nature in visible wavelengths and the energy gap was blue-shifted at Ni = 6 at%. Visible light driven photo-catalytic hydrogen generation with the apparent quantum efficiency around 80% was demonstrated by Khan et al. [37] on $Cd_{0.9}Zn_{0.1}S$. The energy gap of Bi doped $Cd_{0.9}Zn_{0.1}S$ QD was varied between 3.76 and 4.0 eV [38]. Moreover, the maximum PL red intensity was noticed at Bi = 1% doped $Cd_{0.9}Zn_{0.1}S$. The elevated blue light emission and also the red shifted red emission have been noticed on PL examination of Cr, Zn co-doped CdS [39]. Based on the enhanced optical and emission properties, the Zn, Cr co-doped CdS is suitable for the opto-electronic device applications. The photo-catalytic stability investigation signified that Cu added $Cd_{0.9}Zn_{0.1}S$ exhibits better dye elimination ability and enhanced stability even after 6 continuous cycles with limited photo-corrosion owing to more charge carriers release, improved surface to volume ratio and formation of more defects [40].

The Au doped $Cd_{0.25}Zn_{0.75}S$ nanostructures had exhibited 97% of photo-catalytic removal capacity of MB dye which is 20% superior to the $Cd_{0.25}Zn_{0.75}S$ nanostructures [41]. $Zn_{0.3}Cd_{0.7}S$ exhibited the maximum level of photo-catalytic activity and stability for the degradation of MO with $k = 0.85\ h^{-1}$, which is 2.2 times higher than that of CdS [42]. The optical properties of the Zn added CdS revealed that the energy gap of Zn-doped CdS is higher than the energy gap of the pure CdS nanostructures [43]. The photo-current investigation showed that Zn added CdS are better detector in comparison to the pure CdS. The effect of Zn doping on the optical and photovoltaic characteristics of CdS were investigated using UV–Vis, Raman spectroscopy and J–V plots [44]. The band gap of CdS ilms increased from 2.63 to 2.73 eV with the increase of Zn from 2 to 10% [45]. The carrier concentration of Zn doped CdS films at room temperature are found to be in the range of 1019–1020 cm^{-3} suggesting that the prepared films are degenerate semiconductors.

It is found from the literature that no detailed investigation on the photo-catalytic and antibacterial studies of Zn/Ni-doped CdS was made. Therefore, in the current work, $Cd_{0.9}Zn_{0.1}S$ and Ni = 3 wt% doped $Cd_{0.9}Zn_{0.1}S$ have been synthesized by co-precipitation route. Further, the role of Ni on the optical, structural, photo-catalytic and antibacterial properties has been investigated and results were interpreted.

2 Experimental Details

2.1 Synthesis of Ni-Doped $Cd_{0.9}Zn_{0.1}S$ (Ni 3%) Nanostructures

Zn and Ni two element doped CdS nanostructures were prepared using co-precipitation route. Precipitation route have a multiple advantages collectively with the addition of different impurities with various doping levels, and excellent quality control of doping [46].

Cadmium acetate dihydrate ($Cd(CH_3COOH)_2{\cdot}2H_2O$), zinc acetate dihydrate [$Zn(CH_3COO)_2{\cdot}2H_2O$], Nickel acetate tetrahydrate ($Ni(OCOCH_3)_2{\cdot}4H_2O$) and sodium sulfide ($Na_2S$) were used as the precursors without further purification. The entire chemicals employed in the present work were analytical grade (AR) and also high purity (> 99% purity). The chemicals, $Cd(CH_3COOH)_2.2H_2O$, $Zn(CH_3COO)_2{\cdot}2H_2O$, $Ni(CH_3COO)_2{\cdot}4H_2O$ and Na_2S purchased from M/s. Merck chemical Co. were the source of Cd^{2+}, Zn^{2+}, Ni^{2+} and S^{2-} ions, respectively. The preparation method is as discussed in our earlier paper [26]. The flow-chart and the procedures for the preparation of Zn and Ni dual doped CdS nanostructures using chemical precipitation method are as shown in Fig. 1.

The pH value is maintained as 9.2 by the addition of aqueous ammonia solution. A yellow color output was filtered and rinsed a number of times by high purity distilled water and ethanol to remove the pollution. The collected

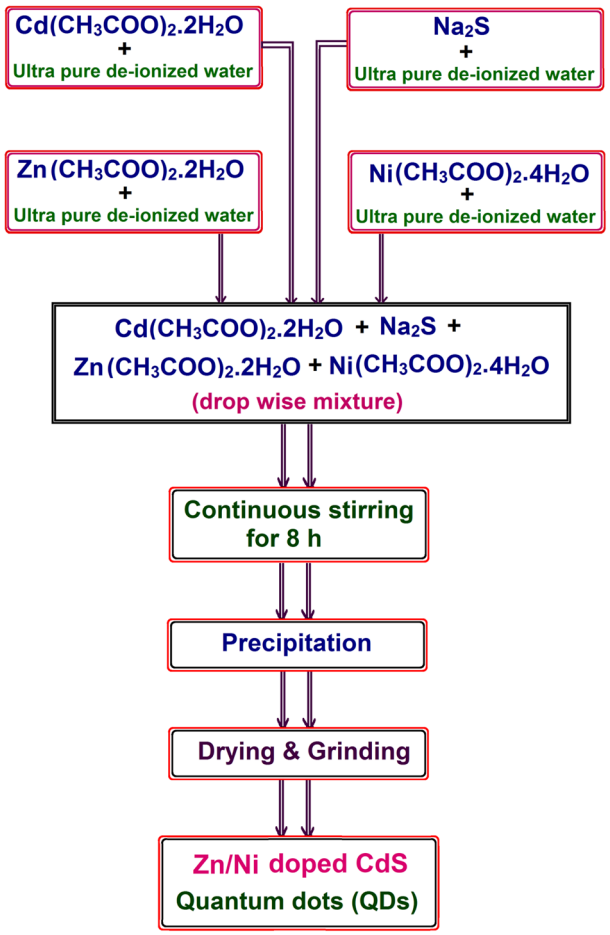

Fig. 1 Flowchart and the preparation steps of Zn and Ni co-doped CdS using chemical precipitation method

precipitates were dried using an oven at 100 °C for 18 h. The similar process was replicated for all the samples. The color of the nanoparticles for Ni = 0% is found to be yellow which is changed to brown for Ni = 3%.

2.2 Characterization Techniques

The diffracted patterns of the synthesized samples have been carried out using RigaKuC/max-2500 diffractometer with Cu Kα radiation from 2θ = 20° to 60° with a scan rate of 0.04°/S. The microstructure was also examined by transmission electron microscopy (TEM, Philips- CM200) in the range of operating voltage as 20–200 kV. With the help of 'image J' software, size of the nanostructures was evaluated. The size of the particle was estimated from the areas assuming spherical shapes and a histogram of size distribution. The presence of constitutional elements like Cd, Ni, Zn and S were confirmed by energy dispersive X-ray (EDX) spectrometer on K and L lines. The optical absorption and transmittance spectra have been obtained using UV–Visible spectrometer (Model: lambda 35, Make: Perkin Elmer) from 300 to 550 nm at ambient temperature with necessary software.

Photo-catalytic activities of the synthesized samples were carried out on methylene blue (MB) using UV–Vis spectrophotometer. MB stock solution (2 mmol) was prepared in de-ionized (DI) water. 50 mL of prepared MB solution (reactant) was taken into a 100 mL beaker and kept on the magnetic stirrer. Subsequently, 10 mg of the catalyst (synthesized samples) was added into the reactant and irradiations were carried out under UV light (wavelength 360 nm, distance 80 mm, power 80 W) under mild stirring. After UV irradiation, 1 mL of the solution was taken out from the solution at certain time intervals (0 to 3 h) and centrifuged to get the upper clear solution.

Antibacterial activity of the prepared nanoparticle was determined using well diffusion method using Mueller Hinton agar media. Mueller Hinton agar media was purchased from Millipore Sigma (catalog no. 70191). After sterilization and solidification process, wells were cut on the Mueller Hinton agar using cork borer. Two bacteria *Staphylococcus aureus* (gram positive derived from ATCC 25923) and *Escherichia coli* (gram negative derived from ATCC 23724) were taken for the study. These bacterial pathogens were swabbed onto the surface of Mueller Hinton agar plates. Wells were impregnated with the test samples of concentration 50 mg/L with norfloxin 10 µg as the standard. The plates were incubated for 30 min to allow the extract to diffuse into the medium. The plates were incubated at 37 °C for 24 h, and then the zone of inhibition was measured in millimeters. Each antibacterial assay was performed in triplicate and mean values were reported.

3 Result and Discussions

3.1 X-Ray Diffraction (XRD)—Structural Studies

Figure 2 represents the XRD profile of $Cd_{0.9}Zn_{0.1}S$ and $Cd_{0.87}Zn_{0.1}Ni_{0.03}S$ nanostructures between 20 and 60°. The existing broadened XRD peaks instead of sharp one indicates the synthesized nanostructures exhibits the particles or grains in the nano-scale dimension. Both samples contain three broaden orientations such as (111), (220) and (311) directions where (111) orientation possesses highest peak intensity than others. After careful background correction and Rietveld refinement of XRD peaks, the observed XRD patterns showed the cubic CdS structure (JCPDS card no.: 10-454) [47]. From the previous literature it is noted that the addition Ni into $Cd_{0.9}Zn_{0.1}S$ lattice induces the mixed phase (both cubic and hexagonal) [46]. Particularly, Dutkova et al. [48] described the changeover of hexagonal structure of CdS into cubic structure by the addition of Zn = 10% into CdS.

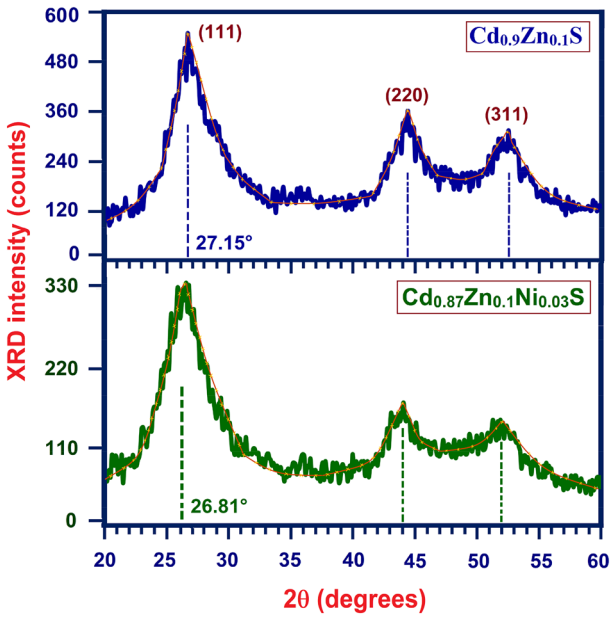

Fig. 2 XRD pattern of $Cd_{0.9}Zn_{0.1}S$ and Ni = 3% doped $Cd_{0.9}Zn_{0.1}S$ between 20 and 60°

In the present work, the XRD spectra confirmed the cubic structure of CdS and also it was altered by the addition of Ni. No additional peaks found in the XRD profile proved the phase purity of the samples without any metal or oxide phases of Zn/Ni in the Cd–Zn–S lattice.

During the addition of Ni = 3% into Cd–Zn–S host lattice, the XRD peak intensity decreased and also the peak position of (111) orientation shifted along the smaller angle side. The noted intensity reduction and the peak position shift by Ni addition reveals the proper replacement of Ni^{2+} instead of Cd^{2+} in Cd–Zn–S lattice. The addition of Ni not only restore Cd^{2+} and also exists as an interstitials which induces structural disorder and defect associated states and are responsible for the modification in peak intensity and position, 2θ [49]. The defect states are related to the chemically prepared nanomaterials as they develop spontaneously at the same of chemical reaction. It may also take place owing to the lack of enough energy required by an atom to shift to an appropriate site in the crystal.

Table 1 illustrates the changes in peak position and FWHM through (111) orientation, cell parameter 'a', 'd' value, mean crystallite size (D) and micro-strain (ε) of $Cd_{0.9}Zn_{0.1}S$ and $Cd_{0.87}Zn_{0.1}Ni_{0.03}S$. Here, the crystallite size is derived from Scherrer relation [50], 0.9 λ/β cosθ. Micro-strain is obtained from the relation [51], β cosθ/4. Both in the calculation of crystallite size and micro-strain, the used parameters β and θ were obtained from (111) orientation. Addition of Ni through Cd–Zn–S lattice, the crystallite size is decreased to 51 Å from 63 Å ($Cd_{0.9}Zn_{0.1}S$). The similar change was noted in Ni–CdS films as reported by Ref. [52]. The shrinkage of size as noticed from Table 1 supports the increase of FWHM and the enhancing micro-strain from 5.471×10^{-3} ($Cd_{0.9}Zn_{0.1}S$) to 6.706×10^{-3} by Ni^{2+} addition. The raise of FWHM could also take place from the micro-straining of the crystals originated from defects like dislocation and twinning. The lattice parameters 'a' and 'c' are increased by the doping of Ni through $Cd_{0.9}Zn_{0.1}S$. The enhanced lattice parameters and the reducing crystallite size were evidenced by Woltersdorf et al. [53].

3.2 Microstructure and Compositional Studies

Figure 3a and b illustrates the typical TEM images of $Cd_{0.9}Zn_{0.1}S$ and Ni = 3% added $Cd_{0.9}Zn_{0.1}S$ samples, respectively. The particle diameters have been evaluated using a histogram of this distribution as shown in Fig. 4. Figure 3a displays the TEM microstructure of $Cd_{0.9}Zn_{0.1}S$ without Ni concentrations; here, shape of the derived grains is almost spherical in nature and they are tightly packed with smooth surface. The particles are well spread inside the sample with the average size around 6 nm (Fig. 4a). Figure 3b displays the TEM image of $Cd_{0.87}Zn_{0.1}Ni_{0.03}S$ sample which exhibits lower crystallite size than the $Cd_{0.9}Zn_{0.1}S$ sample. The reduction in size by Ni in Cd–Zn–S lattice is due to the generation of defect associated lattice disorder. The size of $Cd_{0.87}Zn_{0.1}Ni_{0.03}S$ nanostructure is around ~ 5 nm (Fig. 4b). Moreover, no major changes in shape are observed except the size variation.

For the purpose to investigate the presence of Ni and Zn in CdS, EDX spectra have been performed and Fig. 5 a and b illustrates the EDX measurements of $Cd_{0.9}Zn_{0.1}S$ and Ni = 3% added $Cd_{0.9}Zn_{0.1}S$ samples, respectively. Table 2 describes the changes in quantitative assessment of atomic % of the fundamental elements like Cd, Ni, Zn and S in the prepared samples using EDX spectra. The major EDX peaks

Table 1 The variation of peak position (2θ), FWHM (β) value, d-value, cell parameter 'a', average crystallite size (D) and micro-strain (ε) (along 111 orientation) of $Cd_{0.9-x}Zn_{0.1}Ni_xS$ (x = 0 and 0.03) nanoparticles

Samples	Peak position (2θ) (°)	FWHM (β) (°)	d-value (Å)	Cell parameter a = b = c (Å)	Average crystallite size (D) (Å)	Micro-strain(ε) (10^{-3})
$Cd_{0.9}Zn_{0.1}S$	27.15	1.29	3.28	5.69	63	5.471
$Cd_{0.87}Zn_{0.1}Ni_{0.03}S$	26.81	1.58	3.32	5.76	51	6.706

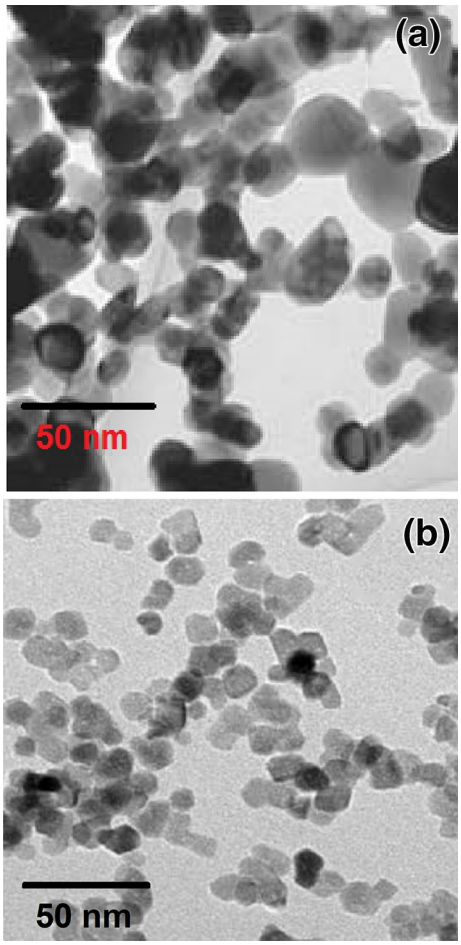

Fig. 3 TEM micrographs of **a** $Cd_{0.9}Zn_{0.1}S$ and **b** Ni = 3% doped $Cd_{0.9}Zn_{0.1}S$

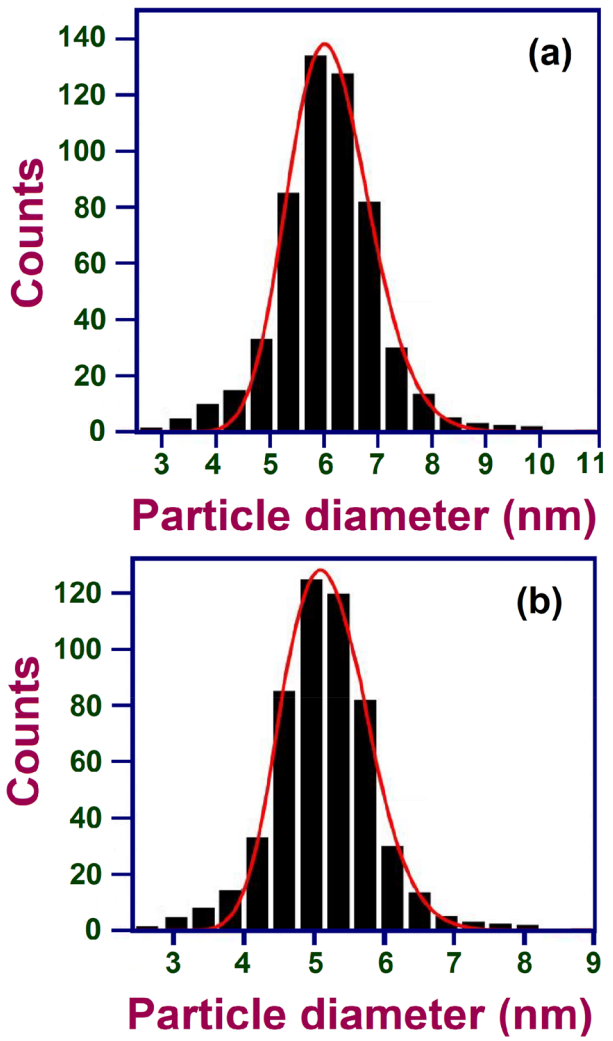

Fig. 4 The estimation of particle diameters using a histogram of TEM distribution **a** $Cd_{0.9}Zn_{0.1}S$ and **b** Ni = 3% doped $Cd_{0.9}Zn_{0.1}S$

validate the elements Zn, Cd, Ni and S. The EDX measurements were taken out at different positions of the nanostructures to enhance the precision of the measurement. It is noted from Fig. 4 that Zn/(Cd + Zn + Ni) ratio is appeared as approximately 10% and the Ni/ (Cd + Zn + Ni) ratio is achieved as 2.93% for Ni = 3% added $Cd_{0.9}Zn_{0.1}S$. The outcome of the results from Table 2 and Fig. 4 suggested that the atomic % of the fundamental elements in the prepared samples coincidence with the amount of initial chemicals used to prepare the samples.

3.3 Optical Absorption and Transmittance Studies

The optical properties and the energy gap of the nanomaterials decide the function and the usage of opto-electronic devices. Figure 6a displays the optical absorption of both $Cd_{0.9}Zn_{0.1}S$ and $Cd_{0.87}Zn_{0.1}Ni_{0.03}S$ from 300 to 550 nm. Figure 6a reflected that Zn = 10% doped CdS ($Cd_{0.9}Zn_{0.1}S$) exhibits single absorption peak centered at 306 nm. $Cd_{0.9}Zn_{0.1}S$ possesses strong absorption below 340 nm without any anomalous absorption in the higher wavelength visible region. The sudden fall down of absorption below 340 nm is responsible for the energy of $Cd_{0.9}Zn_{0.1}S$ nanostructures [54]. The addition of Ni = 3% induces three anomalous absorption peaks; first one centered at 323 nm (corresponding to ~ 3.85 eV), second at 355 nm (~ 3.50 eV) and the third centered around 436 nm (~ 2.85 eV).

In the absorption profile, the first peaks related to UV light and the third peak is accountable for bluish-violet light. In addition to the anomalous absorption generation, absorption edge moved towards larger wavelength side (known as red shift) by the Ni inclusion in $Cd_{0.9}Zn_{0.1}S$ nanostructures. The current red shift i.e., decrease of energy gap by Ni addition was explored by Chandramohan [55]. The present shift along higher wavelength side for Ni doped samples evidently signified that Ni^{2+} ions were substituted into Cd–Zn–S lattice [56].

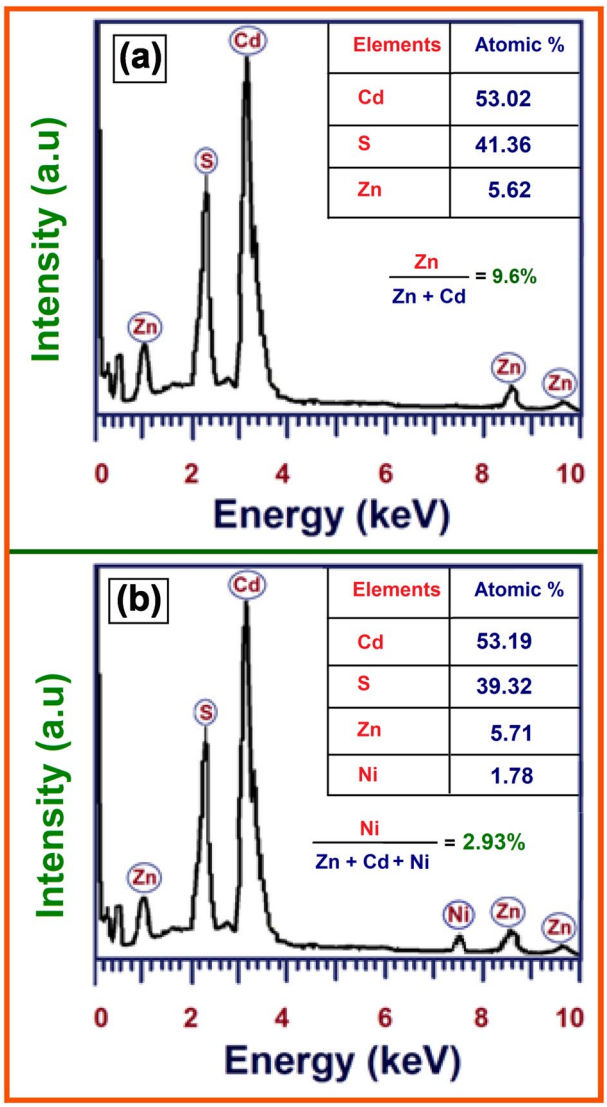

Fig. 5 EDX spectra of **a** $Cd_{0.9}Zn_{0.1}S$ and **b** Ni = 3% doped $Cd_{0.9}Zn_{0.1}S$ nanostructures. The inset shows the constituent elements present in the samples

Table 2 The quantitative analysis of atomic percentage of the compositional elements presents in $Cd_{0.9-x}Zn_{0.1}Ni_xS$ (x = 0 and 0.03) nanoparticles using EDX analysis

Samples	Atomic % of the elements (%)				Ni/(Cd + Zn + Ni) ratio
	Cd	S	Zn	Ni	
$Cd_{0.9}Zn_{0.1}S$	53.02	41.36	5.62	–	–
$Cd_{0.87}Zn_{0.1}Ni_{0.03}S$	53.19	39.32	5.71	1.78	2.93

Generally, the absorption in the UV region i.e., below 380 nm (peaks at 326 and 355 nm) is begins from the electron transitions from valence to conduction bands corresponding to E_g of the nanomaterials [39]. The appearance of

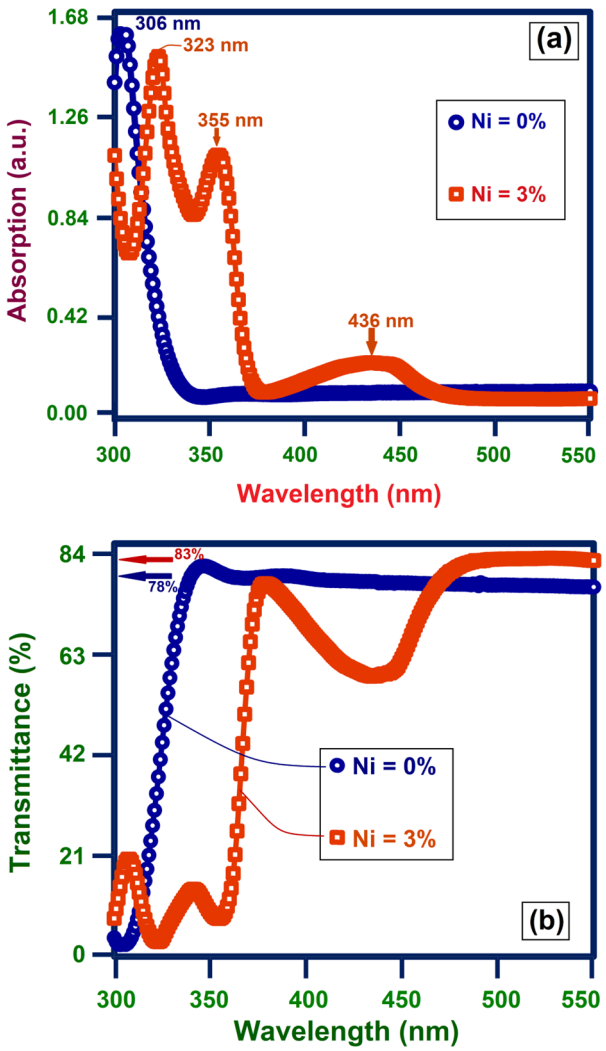

Fig. 6 **a** UV–Visible absorption spectra and **b** transmittance spectra of $Cd_{0.9}Zn_{0.1}S$ and Ni = 3% doped $Cd_{0.9}Zn_{0.1}S$ from 300 to 550 nm

anomalous absorption peaks i.e., more peaks by Ni doping is owing to the establishment of different defects like vacancies, interstitials, etc. [55] which act as trapping centers in the lattice. The visible peak at 436 nm (~bluish violet radiation) is due to the presence of Zn/Cu interstitials in the host lattice. The defects and disorder in the lattice [39] induced by Ni generates the new inter-energy levels in the conduction band [57] and the inter-band transition creates the absorption peak near 436 nm.

Figure 6b represents the transmittance spectra of $Cd_{0.9}Zn_{0.1}S$ and $Cd_{0.87}Zn_{0.1}Ni_{0.03}S$ between 300 and 550 nm. Zn = 10% doped CdS exhibits dominant transmittance in the visible wavelengths and possesses highest transmittance at 78%. At the same time, Ni = 3% doped $Cd_{0.9}Zn_{0.1}S$ sample exhibits relatively higher transmittance of around 83% after 450 nm. The same trend of transmittance was observed by Ouachtari et al. on CdS thin films prepared by CBD method

[58]. The noted relative higher transmittance at Ni doped sample in the visible region suggested them for an efficient transparent window in the solar cells [30].

3.4 Energy Gap (E_g)

The energy gap of Zn = 10% added CdS and Ni = 3% added $Cd_{0.9}Zn_{0.1}S$ samples is derived [59] from the graph, $(\alpha h\upsilon)^2$ versus the energy ($h\upsilon$) Fig. 7 shows the $(\alpha h\upsilon)^2$ versus $h\upsilon$ curves of $Cd_{0.9}Zn_{0.1}S$ and Ni = 3% doped $Cd_{0.9}Zn_{0.1}S$ for energy gap (E_g) calculation. E_g of the above materials is decreased from 3.8 eV ($Cd_{0.9}Zn_{0.1}S$ without Ni concentrations) to 3.38 eV for Ni = 3% added $Cd_{0.9}Zn_{0.1}S$. Here, the derived E_g (~ 3.38–3.8 eV) is higher than normal CdS which exhibits E_g ~ 2.42 eV [60]. The similar enhanced E_g was noted in TM ions added CdS materials due to its reduced spatial nano dimension [61, 62]. We noted from Fig. 6 that E_g possesses considerable decline ($\Delta E_g \approx 0.42$ eV) during the substitution of Ni = 3%. The same declining trend of E_g was described by Senthil [63] in Ni substituted CdS.

Ni^{2+} inclusion produces the extra free charge carriers which are accountable for the E_g reduction. The creation of additional charges is confirmed by the increase of electrical conductivity and decrease of resistance in Ni–Cd–S lattice [30]. The creation of free electrons is named as "free carrier absorption" which is accountable for the present decrease in E_g. Moreover, the noted reducing E_g by Ni addition is induced from the 'p-d' hybridization of Ni/Cd and sulfide in the existence of intermediary energy levels [32] in E_g. The present shrinkage of E_g recognized the existence of Ni^{2+} within Cd–Zn–S lattice [56]. This noticeable reduction in E_g by Ni doping is by the generation of extra energy levels inside the E_g of Cd–Zn–S which broaden the light absorption towards the longer wavelengths [64]. The shrinkage in E_g by Ni addition is explained by the energy level diagram as shown in Fig. 8. The same defect associated reduction in E_g was described by Premarani et al. [65] by the introduction of new energy levels around the two bands in Ni doped system.

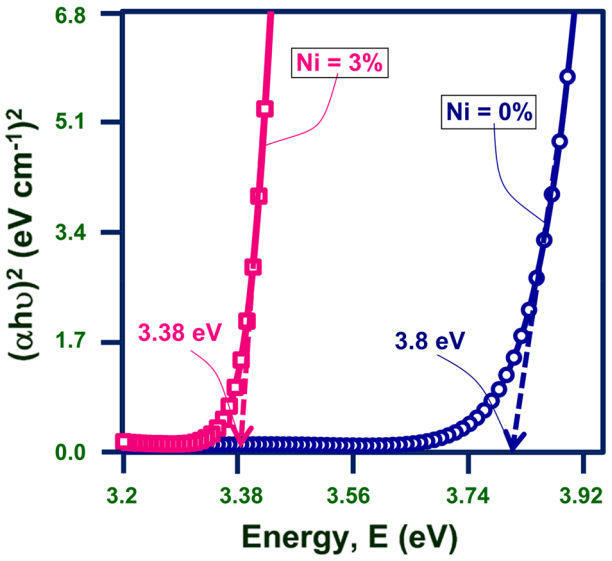

Fig. 7 The $(\alpha h\upsilon)^2$ versus $h\upsilon$ curves of $Cd_{0.9}Zn_{0.1}S$ and Ni = 3% doped $Cd_{0.9}Zn_{0.1}S$ for energy gap calculation

3.5 Photo-Catalytic Studies

MB (odorless and green color chemical) is the major water pollutant discharging from the manufacturing unit like textile industries. It is highly soluble in water and dangerous for the surrounding atmosphere. To eradicate the water pollutant and remove the toxic chemicals from the textile industry wastage, the two metal elements doped CdS is employed as the photo-catalyst. The derived excellent optical properties, smaller size and reducing E_g by Ni addition encouraged the Ni/Zn-CdS nano-system for photo-catalytic applications. Doping of Zn^{2+}/Ni^{2+} in Cd–S modifies the energy levels of the host lattice and so useful for enhancing the efficiency of the photo-catalyst. In this work, toxic removing capacity of the samples such as $Cd_{0.9}Zn_{0.1}S$ and $Cd_{0.87}Zn_{0.1}Ni_{0.03}S$ were evaluated using MB solution within the time 0–120 min. Here, UV radiation is employed as a source. Literature from absorption spectra indicate that the characteristic wavelength of the MB is in the region around 620–660 nm [66, 67].

The dye removing capacity of nano-sized materials is decided by the generation of photo-created electron–hole

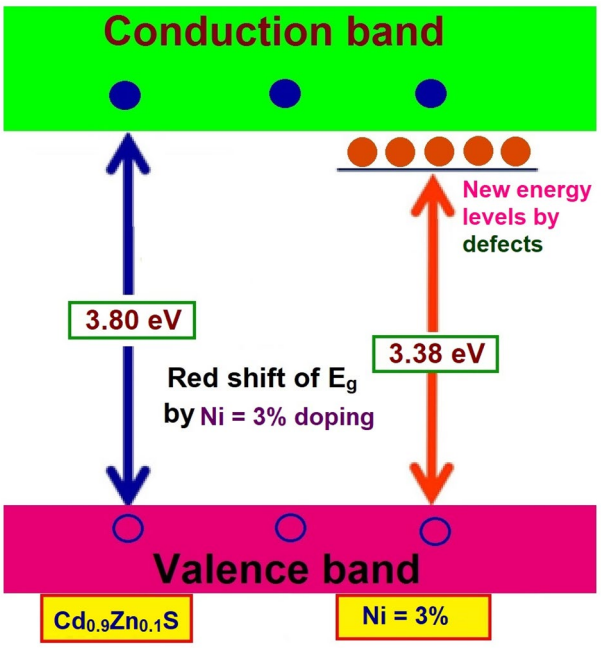

Fig. 8 Energy level graphical diagram to explain the red-shift of E_g in Ni = 3% doped $Cd_{0.9}Zn_{0.1}S$ by the formation of new energy levels by defects

couples [68]. The graphical diagram to explain the mechanism of photo-degradation of the dye using our samples as photo-catalyst by UV light is as shown in Fig. 9. During the irradiation of UV energy as seen in Fig. 8, the electrons from lower energy level are elevated to higher levels by releasing electron–hole couples. As, Ni possesses partially occupied orbital and Ni added Cd–Zn–S exhibits sub-energy levels within the band gap, it can generates more couples (electron–hole) within the energy gap. The noted decrement in E_g from Figs. 7 and 8 by Ni inclusion is the one more support to collect the additional visible radiation and hence the generation of more electron–hole pairs [69]. The presence of metal ions like Ni^{2+} and Zn^{2+}, and the defects such as S^{2-} alter the band structure of CdS and enhance the dye removal efficiency [70].

3.6 Photo-Catalytic Mechanism

Degradation mechanism of MB dye using Zn^{2+}/Ni^{2+}- CdS catalyst is described by the three step reactions [71]:

3.6.1 Step I: Creation of electron–hole couple

$$\text{Zn/Ni doped CdS} + h\upsilon \rightarrow \text{Electron } (e^{-}\text{in CB}) + \text{Hole } \left(h^{+}\text{in VB}\right)$$

3.6.2 Step II: Photo-oxidation and photo-reduction

$$\text{Electrons} + \text{Oxygen molecule } \left(O_2\right) \rightarrow \text{Superoxide free radical } (O_2^{\cdot -}) \text{ (photo - reduction)}$$

$$\text{Holes} + \text{Hydroxyl ion } (OH^{-}) \rightarrow \text{Hydroxyl radical } (OH^{\cdot}) \quad \text{(photo - oxidation)}$$

3.6.3 Step III: De-gradation process

$$\text{Hydroxyl radical } (OH^{\cdot}) + \text{MB} \rightarrow \text{Degradation product}$$

$$\text{Superoxide free radical } (O_2^{\cdot -}) + \text{MB} \rightarrow \text{Degradation product}$$

$$OH^{\cdot} + O_2^{\cdot -} + \text{MB} \rightarrow H_2O + CO_2 \uparrow + SO_4^{2-}$$

In the 1st step electron–hole couple is created during the photo reaction. In the 2nd step, the induced electrons in CB by photon absorption can combine with oxygen molecules and generate the superoxide free radical ($O_2^{\cdot -}$). The released anions further react with H_2O_2 and generate the hydroxyl radicals such as OH^{-}, O_2 and $OH^{\cdot}$. The photo generated holes can react with OH^{-} and generatye the hydroxyl radicals $OH^{\cdot}$. The photo generated species like superoxide free radicals ($O_2^{\cdot -}$), $OH^{\cdot}$ radicals and H_2O_2 acting as chief role in the third step i.e., de-gradation process. The above species combine with MB chemical solution and gives the non-toxic degradation products. During the 3rd step, all the chemical bondings are broken and blue colour MB dye de-colorize into color-less product [72]. At the end of the reaction, MB solution is de-generated as H_2O, CO_2 and SO_4^{2-}.

Figure 10 presents the UV absorption spectra of MB solution containing $Cd_{0.9}Zn_{0.1}S$ and $Cd_{0.87}Zn_{0.1}Ni_{0.03}S$ powders

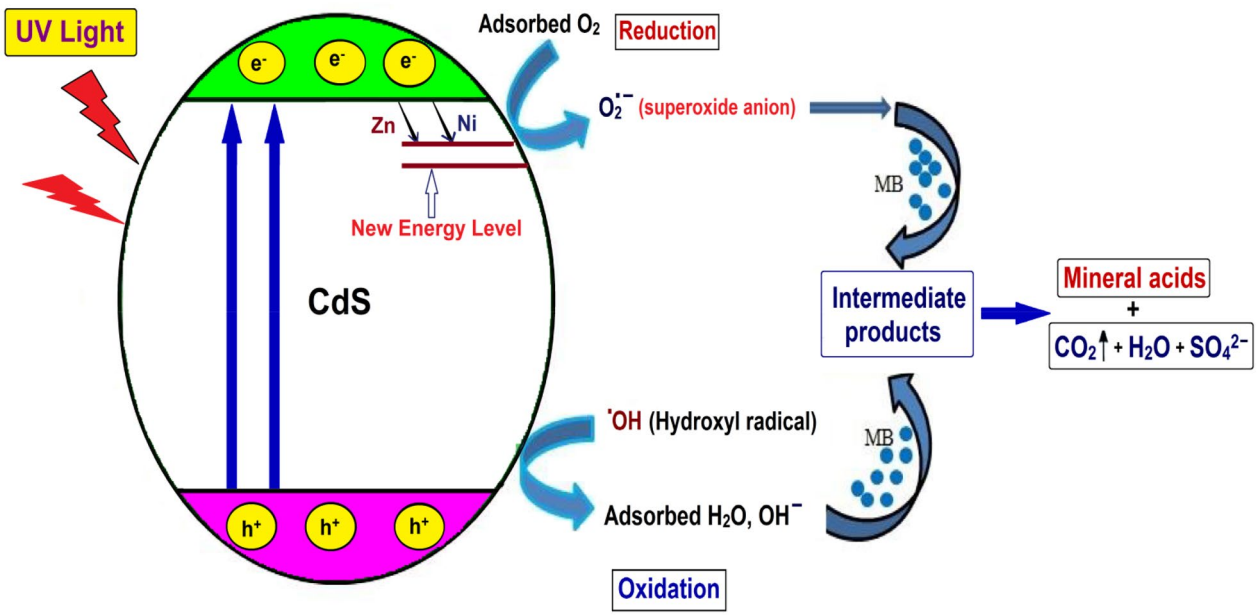

Fig. 9 The graphical diagram to describe the photo-catalytic mechanism of Zn/Ni doped CdS as a catalyst

as catalyst with various UV light exposure time between 0 and 120 min. At initial time (0 min. irradiation), the absorption shows maximum around 660 nm. The intensity falls steadily with the exposure time and reaches minimum at 120 min. The declining absorption intensity around 660 nm is higher for $Cd_{0.87}Zn_{0.1}Ni_{0.03}S$ sample than $Cd_{0.9}Zn_{0.1}S$. To extract the information about the dis-integration of MB solution containing the two synthesized samples, a graphical plot is drawn among the MB concentration fraction (C_t/C_0) versus exposure time (0–120 min.) as shown in Fig. 11a. Figure 11b illustrates the variation of dye removing (degradation) efficiency of MB solution from 0 to 120 min. irradiation times. The dye removing efficiency is obtained by the equation [73], $\eta\ (\%) = [(C_0 - C_t)/C_0] \times 100 = [(A_0 - A_t)/A_0] \times 100$, here, C_0 and C_t are concentration of MB dye solution at the times, '0' and 't' minutes, respectively, and A_0 and A_t are the corresponding absorption values.

The changes in dye removing capacity are explained by the micro-structural and morphological variation and nano-dimension of the catalyst [74]. Figure 10b reflected

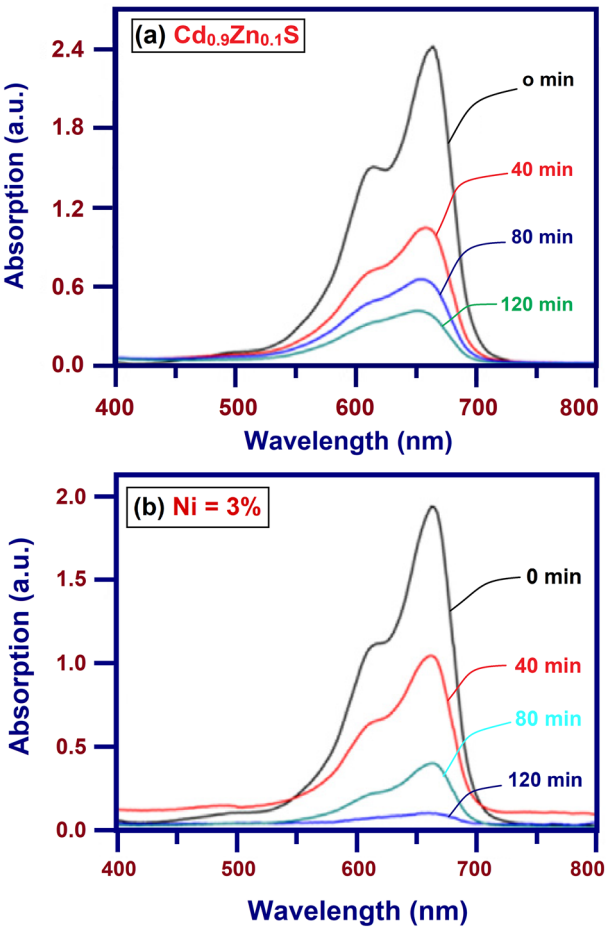

Fig. 10 The variation of absorption intensity of MB solution using **a** $Cd_{0.9}Zn_{0.1}S$ and **b** Ni = 3% doped $Cd_{0.9}Zn_{0.1}S$ as the catalysts between 400 to 800 nm

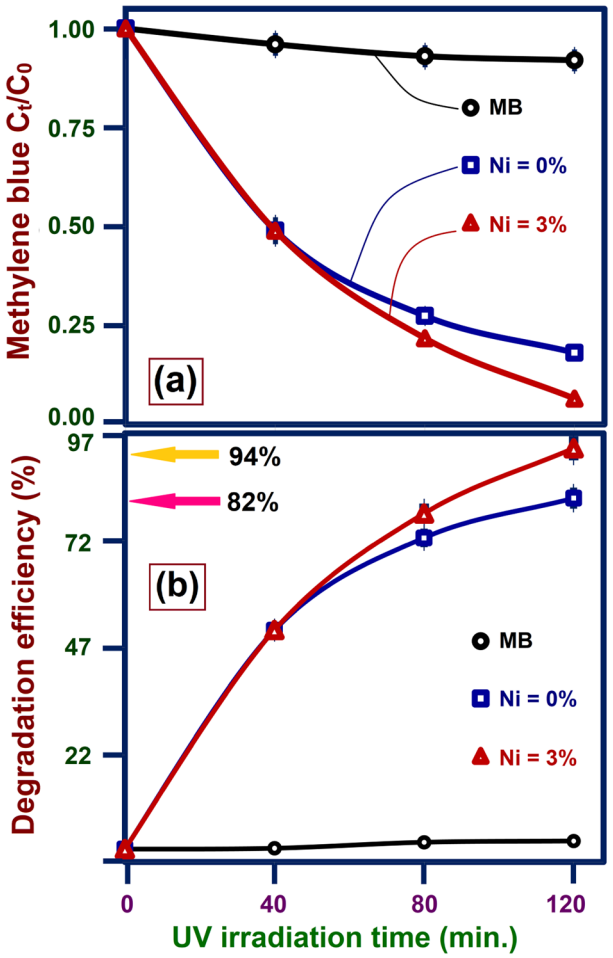

Fig. 11 **a** The concentration ratio (C_t/C_0) versus exposure time profile (0–120 min) and **b** degradation efficiency of MB solution with $Cd_{0.9}Zn_{0.1}S$ and Ni = 3% doped $Cd_{0.9}Zn_{0.1}S$ nanostructures

that $Cd_{0.87}Zn_{0.1}Ni_{0.03}S$ solution exhibits better MB dye removing efficiency than $Cd_{0.9}Zn_{0.1}S$ which may be due to the enhanced surface are and the lower E_g. Table 3 represents the dye removal efficiency of $Cd_{0.9}Zn_{0.1}S$ and $Cd_{0.87}Zn_{0.1}Ni_{0.03}S$ compared with other materials in the literature. The reduced size induces more active sites which enhance the interaction between MB dye and the surface of the catalyst. This interaction improves the photo-catalytic degradation efficiency [81]. The noted better dye removing efficiency in $Cd_{0.87}Zn_{0.1}Ni_{0.03}S$ solution is collective result of charge carrier generation, better optical nature at higher wavelength, enhanced surface area and the stimulation of additional energy levels at the conduction band [82]. To study the mineralization of MB solution, the photo dis-integration study was made by COD (chemical-oxygen-demand) investigation. The percentage of COD reduction is presented in Table 4. After 120 min of UV exposure time with $Cd_{0.87}Zn_{0.1}Ni_{0.03}S$ 94% reduction are received. The

Table 3 The MB dye removing efficiency of $Cd_{0.9}Zn_{0.1}S$ and $Cd_{0.87}Zn_{0.1}Cu_{0.03}S$ compared with other materials with different dyes in the literature

S. No	Samples	Dye chemical	De-gradation efficiency (%)	References
1	$Cd_{0.9}Zn_{0.1}S$	MB	82%	*
2	$Cd_{0.87}Zn_{0.1}Ni_{0.03}S$	MB	94%	*
4	CdS nanoparticles	Reactive red azo dye (RR141)	95% under 240 min visible light	[75]
7	10% Ag–CdS	MB	96.7%	[76]
5	CdS/Ag_2O nanocomposite	MB	88.8%	[77]
3	6% Cu-doped CdS	MB	95% under 210 min UV light 84.5% under 210 min sun light	[78]
6	5% Sn–CdS	MB	96.5%	[76]
9	Ni/Ce doped CdS	MB	90%	[79]
8	$Zn_{1-x}Mn_xS$	MB	50%	[80]

*Current work at 120 min of irradiation time under UV light

Table 4 COD measurement for Ni = 0 and 3% doped $Cd_{0.9}Zn_{0.1}S$ samples between 40 and 120 min. time intervals

S. No	Time (min.)	% of COD reduction: Ni = 0%	% of COD reduction: Ni = 3%
1	40	51	51
2	80	72	78
3	120	82	94

present result suggests that almost the total mineralization of MB was made by $Cd_{0.87}Zn_{0.1}Ni_{0.03}S$.

To investigate the practical application in the factories, the stability i.e., re-usability study is carried out using $Cd_{0.9}Zn_{0.1}S$ and $Cd_{0.87}Zn_{0.1}Ni_{0.03}S$ samples as catalyst for six more runs. Figure 12 illustrates the resultant degradation efficiency at 120 min. exposure time for six re-cycling runs. At end of each run, the output sample is washed several times by de-ionized water and the additional water content is removed using oven at 70 °C for 1–2 h. The sample after cleaning again used for the further cycles. The efficiency of $Cd_{0.87}Zn_{0.1}Ni_{0.03}S$ is derived as 94% at the initial run and it is decreased to 87% for 6th continuous runs. Similarly, $Cd_{0.9}Zn_{0.1}S$ exhibits 82% efficiency at first run and decreased to 76% for 6th run. Figure 12 illustrates the difference in degradation efficiency is ~ 7% for $Cd_{0.87}Zn_{0.1}Ni_{0.03}S$ under six continuous runs which certifies that Ni doped sample have better stability.

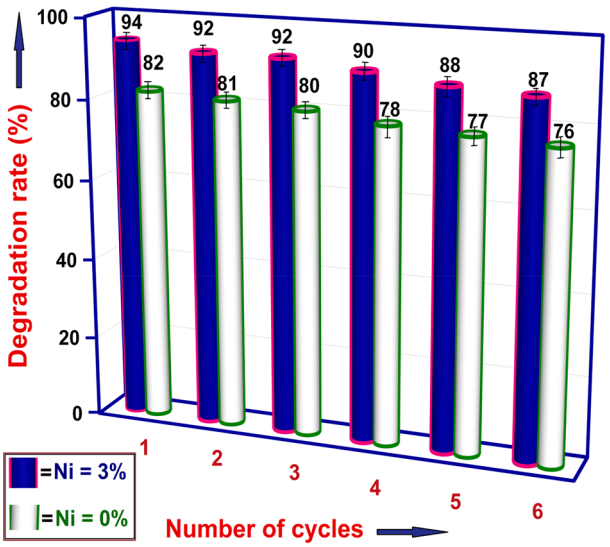

Fig. 12 Investigation of photo-catalytic activity of Zn and Ni co-doped CdS for degradation of MB solution under UV exposure time of 120 min for six runs of degradation reaction

3.7 Antibacterial Studies

The bacterial strains can be classified into main categories as gram-negative and gram positive. The major difference between the two types is the cell structures and the outer cell membranes. It is understand from the literature that the drug or any material depends upon mainly the nature of membranes of bacteria [83]. *S. aureus* and *E. coli* are the two bacterial strains used in the current investigation, the deadly bacteria, which induce various diseases. *S. aureus* and *E. coli* are the Gram-negative and Gram-positive bacteria. Figure 13 displays the zone of inhibition (ZOI) of $Cd_{0.9}Zn_{0.1}S$ and $Cd_{0.87}Zn_{0.1}Ni_{0.03}S$ samples in millimeter (mm) against different bacterial agents such as *S.aureus* (gram + ve) and *E. coli* (gram − ve). Here, ZOI represents the efficiency of bacterial killing capacity and norfloxin is employed as a standard. Figure 14 illustrates the graphical explanation of changes in ZOI for the bacterial strains *S.aureus* and *E. coli*.

Figures 13 and 14 intimated that Ni substituted $Cd_{0.9}Zn_{0.1}S$ provides the superior anti-bacterial activity against the two bacterial agents than $Cd_{0.9}Zn_{0.1}S$ which is mainly due to the variation in the quality of the bacterial cell walls. Both bacterial strains have a − vely charged

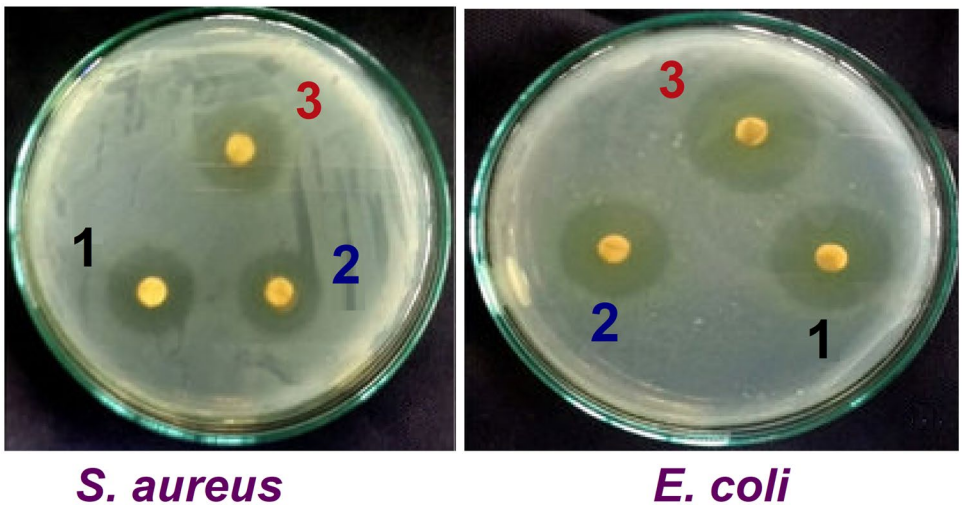

Fig. 13 The zone of inhibition (ZOI) in mm of $Cd_{0.9}Zn_{0.1}S$ and Ni = 3% doped $Cd_{0.9}Zn_{0.1}S$ nanostructures against *S. aureus* and *E. coli* bacterial strains

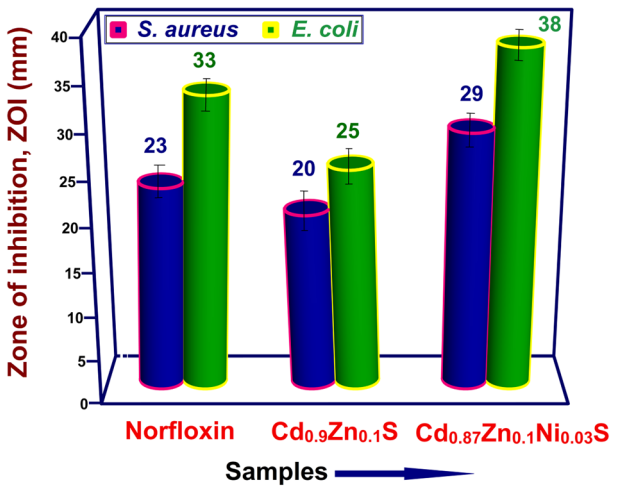

Fig. 14 The graphical representation of ZOI for different micro-organisms such as *S. aureus* and *E. coli* bacterial strains using $Cd_{0.9}Zn_{0.1}S$ and Ni = 3% doped $Cd_{0.9}Zn_{0.1}S$ nanostructures

cell wall. The property that is hypothesizing to influence the relations between the cell walls of the bacterial agents and NPs or + ve charged ions liberated from them. In the present study, CdS releases Cd^{2+} ions whereas, Zn^{2+} and Ni^{2+} ions in aqueous solution paying to the antimicrobial efficiency. The liberated Cd^{2+}, Zn^{2+} and Ni^{2+} ions appreciably contributed to the overall antibacterial result of nano-system [84]. Within the different mechanisms [85, 86] to explore the antibacterial nature, the breakdown of CdS and the reactive oxygen species (ROS) production are believed as the leading mechanism. The metal ions such as Cd^{2+}, Zn^{2+} and Ni^{2+} have superior potential as antibacterial strains attributable to its skill to create ROS.

ROS species like $O_2^{\cdot -}$, H_2O_2 and $OH^{\cdot}$ [87–89] are generated for the period of electron transition from VB to CB. The establishment of ROS is as follows:

$$Zn - Ni - Cd - S + h\upsilon \rightarrow e^- + h^+$$

$$h^+ + H_2O \rightarrow H^+ + OH^{\cdot} \quad \text{(hydroxyl radicals)}$$

$$e^- + O_2^{\cdot} \rightarrow O_2^{\cdot -} \quad \text{(superoxide radical)}$$

$$O_2^{\cdot} + H^+ \rightarrow HO_2^{\cdot}$$

$$HO_2^{\cdot} + e^- \rightarrow HO_2^{\cdot -}$$

$$HO_2^{\cdot -} + H^+ \rightarrow H_2O_2$$

The radicals, $O_2^{\cdot -}$ and $OH^{\cdot}$ are the potential ROS species to control the bacterial strains and generate the poisonous effect to the bacterial agents. Padmavathy [90] described that $O_2^{\cdot -}$ and $OH^{\cdot}$ influence the outside section of the bacterial cell membrane and the radical H_2O_2 is going inside the inner portion of the bacterial cells. Figures 13 and 14 reflected that $Cd_{0.87}Zn_{0.1}Ni_{0.03}S$ displays the better bacterial killing activity than $Cd_{0.9}Zn_{0.1}S$. Mechanism behind the superior bacterial killing capacity at Ni doped sample is explained in Fig. 15. The existence of metal ions like Cd^{2+}, Zn^{2+} and Ni^{2+} are also plays influential role in the antibacterial activity.

The induced ROS by the photo-catalyst reduce the anti-oxidant protection system, inhibit ATP generation and damage the cell membrane. The ROS production is dominantly influenced by the alteration of band structure by Zn^{2+}/Ni^{2+} into CdS. They have the potential to modify the electron transport chain within bacteria. Moreover, H_2O_2 generation also limit the development of bacteria [91, 92]. The higher anti-bacterial killing efficiency at $Cd_{0.87}Zn_{0.1}Ni_{0.03}S$

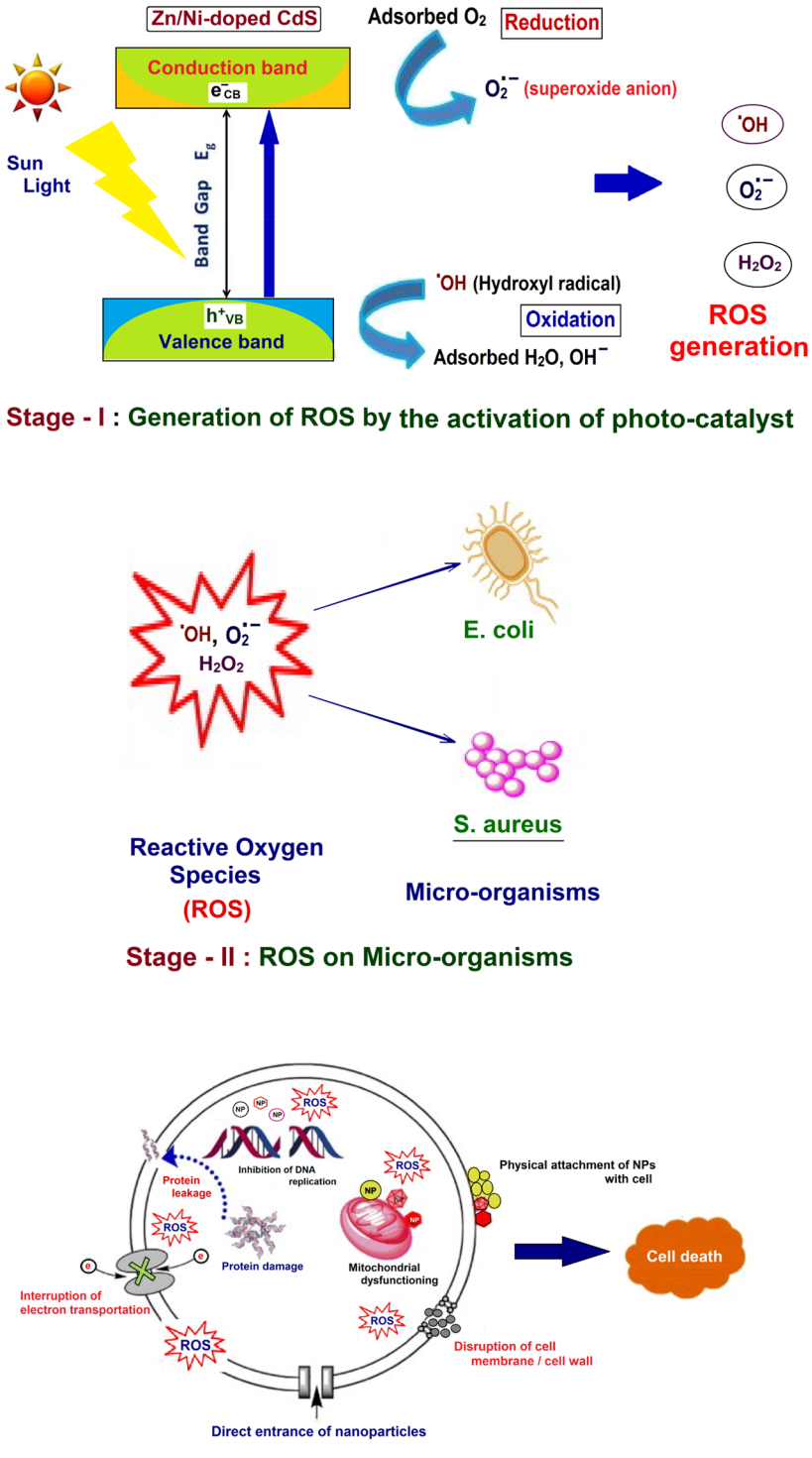

Fig. 15 The graphical representation of mechanism behind the antibacterial activity of Ni = 3% doped $Cd_{0.9}Zn_{0.1}S$ nanostructures with three different stages

may be from the reduced size i.e., increased surface area and also more ROS generating ability [93]. The ROS and the positive charged ions accelerate the dis-integration of cell walls which enhances the leakage of cell elements and forces the cell death [94, 95]. The graphical representation of mechanism behind the antibacterial activity of Ni = 3% doped $Cd_{0.9}Zn_{0.1}S$ nanostructures with three different stages is illustrated in Fig. 15.

The release of metal ions (Cd^{2+}, Zn^{2+} and Ni^{2+}) also inhibit the bacterial agents. The + ve ions are attracted by – ve charged bacterial cells and hence they enter easily the cell wall of the bacteria and react through—SH clusters

present in the wall. This reaction guides the death of the bacterial [73]. It is understand from Fig. 14 that *E. coli* bacteria show better anti-bacterial efficiency than *S. aureus*. Even though all bacteria possess internal cell wall, *E. coli* holds a distinctive external wall which forbids the drugs and antibiotics and hence decreases the cell damage. The presence of unique cell wall in *E. coli* is accountable for accomplishment more antibacterial efficiency than *S. aureus* bacteria. Vanaja et al. [96] also noticed the higher ZOI using silver as a catalyst at gram negative strains than the gram positive strains owing to the variation in the bacteria cell wall.

4 Conclusions

$Cd_{0.9}Zn_{0.1}S$ and $Cd_{0.87}Zn_{0.1}Ni_{0.03}S$ were prepared by chemical co-precipitation method. The XRD profile proved the cubic crystal structure of the samples without any impurity related phases and no changes in the cubic phase were noted by Zn/Ni doping in CdS. The reduced size from 63 to 51 Å and the dissimilarities in lattice parameters and micro-strain has been discussed by Ni addition and the defects connected with Ni^{2+}. The noticed anomalous absorption bands in the visible wavelength and the elevated transmittance at Ni doped sample suggested that the synthesized materials are useful for the fabrication of efficient opto-electronic devices. The band gap reduction during the substitution of Ni = 3% is explained by the generation of extra energy levels associated with defects within the two bands. The release of additional charge carriers, improved optical property, reduced particle size and more defect generation are responsible for the enhanced photo-catalytic performance of Ni doped $Cd_{0.9}Zn_{0.1}S$. The photo dis-integration was also confirmed by COD study which affirms the complete mineralization of MB solution. The photo-catalytic re-cycling study confirmed the stability of Ni doped $Cd_{0.9}Zn_{0.1}S$ for six cycle runs. The enhanced anti-bacterial capacity in $Cd_{0.87}Zn_{0.1}Ni_{0.03}S$ is described by the collective response of reduced particle size and higher ROS generating capacity.

References

1. P.S. Kumar, M. Selvakumar, S.G. Babu, S. Karuthapandian, Mater. Res. Bull. **83**, 522–533 (2016)
2. Y. Yina, J. Li, Y. Wang, J. Wan, X. Du, X. Hu, E. Liu, J. Fan, Mater. Res. Bull. **88**, 33–40 (2017)
3. S. Verma, R.B.N. Baig, M.N. Nadagouda, R.S. Varma, Green Chem. **18**, 1327–1331 (2016)
4. D. Chauhan, P. Kumar, C. Joshi, N. Labhsetwar, S.K. Ganguly, S.L. Jain, New J. Chem. **39**, 6193–6200 (2015)
5. S. Verma, R.B.N. Baig, M.N. Nadagouda, R.S. Varma, Chem. Catal. Chem. **8**, 690–693 (2016)
6. Y. Shiraishi, D. Togawa, D. Tsukamoto, S. Tanaka, T. Hirai, ACS Catal. **2**, 2475–2481 (2012)
7. J. Zhang, Y. Wang, J. Zhang, Z. Lin, F. Huang, J. Yu, ACS Appl. Mater. Interfaces **5**, 1031–1037 (2013)
8. Q. Deng, X. Duan, D.H.L. Ng, H. Tang, Y. Yang, M. Kong, Z. Wu, W. Cai, G. Wang, ACS Appl. Mater. Interfaces **4**, 6030–6037 (2012)
9. S. Ghasemi, S.J. Hashemian, A.A. Alamolhoda, I. Gocheva, S.R. Setayesh, Mater. Res. Bull. **87**, 40–47 (2017)
10. R.B.N. Baig, S. Verma, R.S. Varma, M.N. Nadagouda, A.C.S. Sustain, Chem. Eng. **4**, 1661–1664 (2016)
11. P. Kumar, S. Varma, S.L. Jain, J. Mater. Chem. A **2**, 4514–4519 (2014)
12. P.C. Dey, R. Das, Spectrochim Acta A **207**, 156–163 (2019)
13. C. Malarkodi, S. Rajeshkumar, K. Paulkumar, M. Vanaja, G. Gnanajobith, G. Annadurai, Bioinorg. Chem. Appl. **2014**, 347167 (2014)
14. A. Sundari, A. Shrivastav, B. Vijay, R. Soni, S. Goyal, R. Meshugga, Macromol. Symp. **357**, 223–228 (2015)
15. P.C. Dey, R. Das, J. Lumin. **183**, 368–376 (2017)
16. G. Petre, I. Pintilie, E. Pentia, I. Pintilie, T. Botila, Mater. Sci. Eng. B **58**, 238–243 (1999)
17. A. Nag, S. Sapra, S.S. Gupta, A. Prakash, A. Ghangrekar, N. Periasamy, Bull. Mater. Sci. **31**, 561–568 (2008)
18. S.M. Taheri, M.H. Yousefi, Braz. J. Phys. **40**, 301–305 (2010)
19. O. Lehmann, K. Kompe, M. Haase, J. Am. Chem. Soc. **126**, 14935–14942 (2004)
20. L. Zu, D.J. Norris, T.A. Kennedy, S.C. Erwin, A.L. Efros, Nano Lett. **6**, 15334 (2006)
21. X. Huang, A. Makmal, J.R. Chelikowsky, L. Kronik, Phys. Rev. Lett. **94**, 236801 (2005)
22. V. Narasimman, V.S. Nagarethinam, K. Usharani, A.R. Balu, Int. J. Thin. Film Sci. Technol. **5**, 17–24 (2016)
23. H. Sekhar, D.N. Rao, J. Mater. Sci. **47**, 1964–1971 (2012)
24. M. Anpo, M. Takeuchi, J. Catal. **216**, 505–516 (2003)
25. E. Zych, D. Hreniak, W. Strek, J. Phys. Chem. B **106**, 3805–3812 (2002)
26. I. Devadoss, S. Muthukumaran, M. Ashokkumar, J. Mater. Sci.: Mater. Electron. **25**, 3308–3317 (2014)
27. R. Chauhan, A. Kumar, R.P. Chaudhary, Appl. Surf. Sci. **270**, 655–660 (2013)
28. S.K. Mishra, R.K. Srivastava, S. Prakash, R.S. Yadav, A. Panday, J. Alloys Compd. **513**, 118–124 (2012)
29. S.R. Krishnakumar, N. Shanthi, D. Sarma, Phys. Rev. B **66**, 115105 (2002)
30. A. Rmili, F. Ouachtari, A. Bouaoud, A. Louardi, T. Chtouki, B. Elidrissi, H. Erguig, J. Alloys Compd. **557**, 53–59 (2013)
31. A. Pareek, R. Thotakuri, R. Dom, H.G. Kim, P.H. Borse, Int. J. Hydrogen Energy **42**, 125–132 (2017)
32. M.A. Kamran, R.B. Liu, L.J. Shi, B.S. Zou, J. Phys. Chem. C **117**, 17777–17785 (2013)
33. M. Sankar, M. Jothibas, A. Muthuvel, A. Rajeshwari, S. Johnson Jeyakumar, Surf. Interfaces **21**, 100775 (2020)
34. T. Garmim, E. Bouabdalli, L. Soussi, Z. El Jouad, R. Mghaiouini, A. Louardi, B. Hartiti, M. El Jouad, M. Monkade, Phys. Scr. **96**, 045813 (2021)
35. P. Raju, J.P. Jesuraj, S. Muthukumaran, J. Mater. Sci. Mater. Electron. **32**, 14310–14327 (2021)
36. P. Sakthivel, I. Devadoss, A. Krishnamoorthy, J. Phys. Conf. Ser. **1964**, 062103 (2021). https://doi.org/10.1088/1742-6596/1964/6/062103
37. K. Khan, X. Tao, M. Shi, B. Zeng, Z. Feng, C. Li, R. Li, Adv. Funct. Mater. **30**, 2003731 (2020). https://doi.org/10.1002/adfm.202009444
38. A. Krishnamoorthy, P. Sakthivel, I. Devadoss, V.M. Anitha Rajathi, SN Appl. Sci. **3**, 694 (2021). https://doi.org/10.1007/s42452-021-04681-7

39. I. Devadoss, P. Sakthivel, S. Muthukumaran, N. Sudhakar, Ceram. Int. **45**, 3833–3838 (2019)
40. P. Raju, J.P. Jesuraj, S. Muthukumaran, J. Inorg. Organomet. Polym. (2021). https://doi.org/10.1007/s10904-021-02058-2
41. P.P. Gotipamul, K.D. Rajan, S. Khanna, M. Rathinam, S. Chidambaram, J. Mater. Sci.: Mater. Electron. (2021). https://doi.org/10.1007/s10854-021-06279-6
42. L. Yang, M. Zhang, M. Liu, Y. Fan, H. Ben, L. Li, X. Fu, S. Chen, Catalysts **10**, 276 (2020). https://doi.org/10.3390/catal10030276
43. M.A. Baghchesara, R. Yousefi, M. Cheraghizade, F. Jamali-Sheini, A. Sáaedi, Ceram. Int. **42**, 1891–1896 (2016)
44. E. Alisangari, A. Hassanpour, Opt. Quant. Electron. **49**, 340 (2017). https://doi.org/10.1007/s11082-017-1177-2
45. V.V.P. Munaga, T. Krishnan, R.K. Borra, SN Appl. Sci. **2**, 552 (2020). https://doi.org/10.1007/s42452-020-2358-3
46. A. Firdous, D. Singh, M.M. Ahmad, Appl. Nanosci. **3**, 13–18 (2013)
47. Z. Sedaghat, N. Tagavinia, M. Marandi, J. Nanotechnol. **17**, 3812 (2006)
48. E. Dutkova, P. Balaz, P. Pourghahramani, A.V. Nguyen, V. Sepelak, A. Feldhoff, J. Kovac, A. Satka, Solid State Ion. **179**, 1242–1245 (2008)
49. X.L. Yang, Z.T. Chen, C.D. Wang, Y. Zhang, X.D. Pei, Z.J. Yang, G.Y. Zhang, Z.B. Ding, K. Wang, S.D. Yao, J. Appl. Phys. **105**, 053910 (2009)
50. C. Prabakar, S. Muthukumaran, V. Raja, Chem. Phys. Impact **2**, 100019 (2021). https://doi.org/10.1016/j.chphi.2021.100019
51. P. Gokula Krishnan, S. Muthukumaran, V. Raja, J. Lumin. **238**, 118258 (2021). https://doi.org/10.1016/j.jlumin.2021.118258
52. T. Sivaraman, V. Narasimman, V.S. Nagarethinam, A.R. Balu, Prog. Nat. Sci. Mater. Int. **25**, 392–398 (2015)
53. J. Woltersdorf, A. Nepijko, E. Pippel, Surf. Sci. **106**, 64–69 (1981)
54. M.N. Siddique, T. Ali, A. Ahmed, P. Tripathi, Nano-Struct. Nano-Objects **16**, 156–166 (2018)
55. S. Chandramohan, T. Strache, S.N. Sarangi, R. Sathyamoorthy, T. Som, Mater. Sci. Eng. B **171**, 16–19 (2010)
56. M. Thambidurai, N. Muthukumarasamy, S. Agilan, N.S. Arul, N. Murugan, R. Balasundara prabhu, J. Mater. Sci. **46**, 3200–3206 (2010)
57. M. Fox, *Optical Properties of Solids* (Oxford University Press, Oxford, 2001)
58. F. Ouachtari, A. Rmili, B. Elidrissi, A. Bouaoud, H. Erguig, P. Elies, J. Mod. Phys. **2**, 1073–1082 (2011)
59. J. Tauc, *Amorphous and Liquid Semiconductors* (Plenum Press, New York, 1974), p. 159
60. K.S. Kumar, A. Divya, P.S. Reddy, Appl. Surf. Sci. **257**, 9515–9518 (2011)
61. M. Elango, K. Gopalakrishnan, S. Vairam, M. Thamilselvan, J. Alloys Compd. **538**, 48–55 (2012)
62. C.S. Tiwary, R. Sarkar, P. Kumbhakar, A.K. Mitr, Phys. Lett. A **372**, 5825–5830 (2008)
63. K. Senthil, D. Mangalaraj, S.K. Narayandass, B. Hong, Y. Roh, C.S. Park, J. Yi, Semicond. Sci. Technol. **17**, 97–103 (2002)
64. S.G. Ghugal, R.R. Mahalik, P.S. Charde, S.S. Umare, S.B. Kokane, V. Sudarsan, R. Sasikala, Microporous Mesoporous Mater. **242**, 284–293 (2017)
65. R. Premarani, J.J. Devadasan, S. Saravanakumar, R. Chandramohan, T. Mahalingam, J. Mater. Sci. Mater. Electron. **26**, 2059–2065 (2015)
66. A. Rahman, M.T.M. Ayob, S. Radiman, J. Nanotechnol. **2014**, 212694 (2014). https://doi.org/10.1155/2014/212694
67. S.O. Fatin, H.N. Lim, W.T. Tan, N.M. Huang, Int. J. Electrochem. Sci. **7**, 9074–9084 (2012)
68. C.B. Ong, L.Y. Ng, A.W. Mohammad, Renew. Sustain. Energy Rev. **81**, 536–551 (2018)
69. R.M. Navarro, M.C. Alvarez-Galvan, J.A.V. de la Mano, S.M. Al-Zahranib, J.L.G. Fierro, Energy Environ. Sci. **3**, 1865–1882 (2010)
70. B. Ahmed, A.K. Ojha, S. Kumar, Spectrochim. Acta A Mol. Biomol. Spectrosc. **179**, 144–154 (2017)
71. A. Ali, X. Zhao, A. Ali, L. Duan, H. Niu, C. Peng, Y. Wang, S. Hou, Superlatt. Microstruct. **83**, 422–430 (2015)
72. K. Thongsuriwong, P. Amornpitoksuk, S. Suwanboon, J. Sol-Gel Sci. Technol. **62**, 304–312 (2012)
73. K. Karthik, S. Dhanuskodi, S. Prabukumar, C. Gobinath, S. Sivaramakrishnan, J. Mater. Sci.: Mater. Electron. **29**, 5459–5471 (2018)
74. K. Milenova, I. Stambolova, V. Blaskov, A. Eliyas, S. Vassilev, M. Shipochka, J. Chem. Technol. Metal. **48**, 259–264 (2013)
75. T. Senasu, S. Nanan, J. Mater. Sci. Mater. Electron. **28**, 17421–17441 (2017)
76. B. Mullamuri, V.S.S. Mosali, H. Maseed, S.S. Majety, B. Chandu, Biointerface Res. Appl. Chem. **11**, 12547–12559 (2021)
77. P.J. Sophia, D. Balaji, T.J.C. Peters, D.S. Chander, S.V. Rishaban, P.V. Shanthi, K.R. Nagavenkatesh, M.R. Kumar, Chem Select **5**, 4125–4135 (2020). https://doi.org/10.1002/slct.202000475
78. M. Shaban, M. Mustafa, A.M. El Sayed, Mater. Sci. Semicond. Process. **56**, 329–343 (2016)
79. G.P. Rathod, B.M. Kotecha, R. Sharma, H. Amin, P.K. Prajapati, Int. J. Pharm. Biol. Arch. **3**, 582–586 (2012)
80. A.P. Davis, Y.H. Hsieh, C.P. Huang, Chemosphere **31**, 3093–3104 (1995). https://doi.org/10.1016/0045-6535(95)00168-8
81. M. Rezapour, N. Talebian, Mater. Chem. Phys. **129**, 249–255 (2011)
82. R.C. Pawar, C.S. Lee, Appl. Catal. B Environ. **144**, 57–65 (2014)
83. P.C. Dey, B. Ingti, A. Bhattacharjee, M.D. Choudhury, R. Das, S.S. Nath, J. Basic Microbiol. **61**, 27–36 (2021). https://doi.org/10.1002/jobm.202000296
84. A. Chauhan, R. Verma, S. Kumari, A. Sharma, P. Shandilya, X. Li, K.M. Batoo, A. Imran, S. Kulshrestha, R. Kumar, Sci. Rep. **10**, 7881 (2020). https://doi.org/10.1038/s41598-020-64419-0
85. P.K. Stoimenov, R.L. Klinger, G.L. Marchin, K.J. Klabunde, Langmuir **18**, 6679–6686 (2002)
86. L. Zhang, Y. Jiang, Y. Ding, M. Povey, D. York, Nanopart. Res. **9**, 479–489 (2007)
87. T.K. Rahul, N. Sandhyarani, Nanoscale **7**, 18259–18270 (2015)
88. R. Fagan, D.E. McCormack, D.D. Dionysiou, S.C. Pillai, Mater. Semicond. Process. **42**, 2–14 (2015)
89. M. Pelaez, N.T. Nolan, S.C. Pillai, M.K. Seery, P. Falaras, A.G. Kontos, P.S.M. Dunlop, J.W.J. Hamilton, J. Byrne, K. O'shea, M.H. Entezari, D.D. Dionysiou, Appl. Catal. B **125**, 331–349 (2012)
90. N. Padmavathy, R. Vijayaraghavan, Sci. Technol. Adv. Mater. **9**, 1–7 (2008)
91. H. Shivapratap, T. Philip, D. Sharma, Indian J. Seric. **35**, 107–110 (1996)
92. H. Yang, Y.-Y. Ren, T. Wang, C. Wang, Results Phys. **6**, 299–304 (2016)
93. Z.M. Xiu, Q.B. Zhang, H.L. Puppala, V.L. Colvin, P.J.J. Alvarez, Nano Lett. **12**, 4271–4275 (2012)
94. R. Menaka, R. Subiya, Int. J. Sci. Res. **5**, 269–271 (2016)
95. M. Chandrasekaran, K.D. Kim, S.C. Chun, Processes **8**, 1173 (2020). https://doi.org/10.3390/pr8091173
96. M. Vanaja, G. Gnanajobitha, K. Paulkumar, S. Rajeshkumar, C. Malarkodi, G. Annadurai, J. Nanostruct. Chem. **3**, 3–17 (2013)